nature catalysis

Article

https://doi.org/10.1038/s41929-026-01613-9

Consequences of overtones in Raman spectra for assigning nickel anode surface structures as NiO_2 during alkaline electrolysis

Received: 25 November 2025

Accepted: 19 August 2026

Published online: 11 September 2026

Check for updates

Justus Leist[1], Annika Neufischer[1], Timo Jacob[1,2,3] & Albert K. Engstfeld[1]

Ni-based anodes are among the most active and cost-effective oxygen evolution reaction catalysts for alkaline electrolysis. The current mechanistic understanding assumes that the anode surface is terminated by nickel oxohydroxide (NiOOH) under operating conditions. Here, by combining isotope-labelled in situ surface-enhanced Raman spectroscopy measurements with density functional theory-calculated Raman spectra, we elucidate that the catalytically active surface is exclusively terminated by nickel dioxide (NiO_2) instead. Furthermore, bands previously assigned to superoxides are attributed to overtones and combination bands. On the basis of additional measurements on Co- and Mn-based oxides, we suggest that these features predominantly appear in layered materials. Moreover, the observed shifts at varying pH, potentials and electrolyte composition are rationalized by a vibrational Stark effect rather than by changes in the material or adsorbate structure. Finally, the implications for the mechanistic interpretation of the oxygen evolution reaction on Ni-based anodes are discussed on the basis of the revised structural assignment.

Raman spectroscopy is a versatile technique used for chemical, biological (medical) and materials characterization[1,2]. A further advantage is that materials immersed in aqueous environments can be probed in operando. Hence, the technique is indispensable for investigating catalysts under reaction conditions and for resolving reaction mechanisms at the atomic scale[3–5]. Especially under in operando conditions, an enhancement of signal intensities is desired, which can be achieved by plasmon-enhanced Raman spectroscopy (PERS) approaches, including surface-enhanced Raman spectroscopy (SERS)[4–7].

In some cases, the enhancement effect reveals additional bands. These further complicate the already complex interpretation of the spectra and, thus, require additional methods, including density functional theory (DFT) calculations[2]. Furthermore, in Raman spectroscopy and PERS, only fundamental modes are generally observable, as described by the selection rules in the harmonic approximation[8]. However, under certain circumstances, the appearance of overtones and combination bands can be observed, such as for graphene[9] and MoS_2 (ref. 10). The fact that overtones are usually not covered (or even mentioned) in more general reviews on PERS, including recent works on in situ and ambient pressure characterization of solid materials[1–5,7] raises the question of whether such bands might have been overlooked in some research areas.

Ni (oxo)hydroxides are widely discussed oxygen evolution reaction (OER) catalysts for application in alkaline electrolysers[11,12]. On the basis of current understanding, it is accepted that, under OER conditions, Ni electrodes are oxidized to NiOOH[13,14]. Nevertheless, some puzzles related to the structural properties remain, which if clarified, would have implications for the description of the reaction mechanism on this surface. For example, the position of the hydrogen atoms is still debated[15–17], including studies suggesting the presence of delocalized and labile hydrogen atoms[18,19]. Furthermore, it was shown that NiOOH consists of sheets of double hydroxide layers, appearing in two distinct phases (β- and γ-NiOOH). The β-NiOOH phase exhibits a relatively high degree of crystallinity, where Ni is commonly suggested to be

[1]Institute of Electrochemistry, Ulm University, Ulm, Germany. [2]Department of Electrochemistry II and Theory I, Helmholtz-Institute Ulm, Ulm, Germany. [3]Karlsruhe Institute of Technology, Karlsruhe, Germany. e-mail: timo.jacob@uni-ulm.de; albert.engstfeld@uni-ulm.de

https://doi.org/10.1038/s41929-026-01613-9

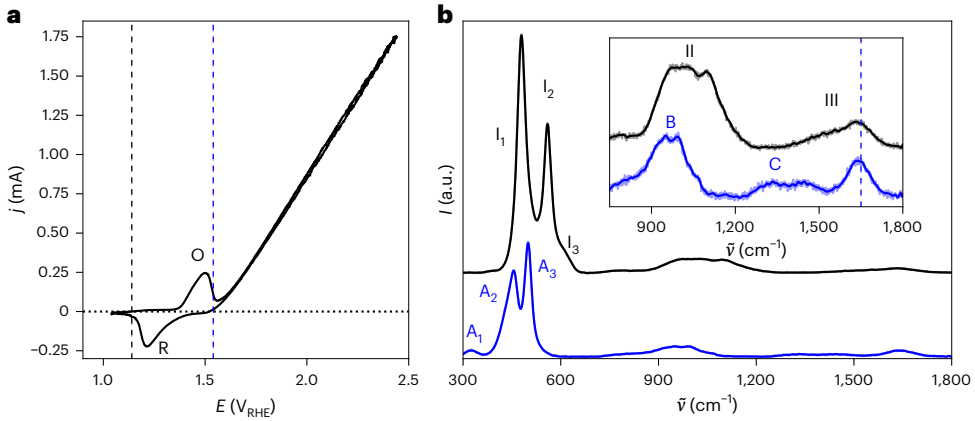

Fig. 1 | Cyclic voltammogram and surface-enhanced Raman spectra of a Ni film supported on a Au wire. a, A cyclic voltammogram for a Au@Ni wire recorded in stirred 0.01 M KOH at a scan rate of 5 mV s^{-1} and limits of 1.04 V_{RHE} and 2.44 V_{RHE}. *j*, current; *E*(V_{RHE}), potential vs. the reversible hydrogen electrode. **b**, In situ SER spectra for Ni in 0.01 M KOH, recorded at electrode potentials of 1.14 V_{RHE} and 1.54 V_{RHE}, at which $Ni(OH)_2$ or NiOOH is formed, respectively. The electrode potentials during both surface-enhanced Raman spectroscopy measurements are marked in **a**. The inset shows the region between 800 and 1,800 cm^{-1} magnified by a factor of 10. The labels I_1, I_2 and I_3 refer to the three peaks of the first region at 479, 560 and 610 cm^{-1} of NiOOH, whereas II and III refer to the two regions at 900–1,200 cm^{-1} and 1,400–1,800 cm^{-1}. The position of the H_2O bending vibration is highlighted in blue for both $Ni(OH)_2$ and NiOOH. *I*, intensity; $\tilde{\nu}$, Raman shift.

in the oxidation state 3.0 (refs. 13,14,20). In contrast, the disordered γ-NiOOH has been reported to be partially deprotonated and to contain intercalated water or cations, such as K^+ (refs. 13,14,21). The oxidation state of Ni in this material has been reported to range between 3.3 and 3.7, suggesting that Ni(IV) is present[13,20,22]. Moreover, according to experimental and computational Pourbaix diagrams, a NiO_2 phase is consistently proposed to be the thermodynamically favoured phase at high pH and high potentials, that is, in the OER region[23–25]. Additionally, in recent SERS studies on NiOOH, an additional band that was reported under OER conditions could not be attributed to the bulk structure but rather to the formation of superoxides on the NiOOH surface[26,27].

To shed some light on these prevailing discrepancies, we first summarize the current understanding of the structural properties of Ni (oxo) hydroxides before and during the OER, in comparison with experimental in situ SERS measurements performed in commonly used electrolytes with varying pH, cation species and isotope composition. Further, we illustrate that assigning DFT-computed NiOOH and NiO_2 Raman spectra is not straightforward and requires insights from experimental data (isotope-labelled SERS measurements in this work and experimental works reporting structural data for these materials). Combining these, we suggest that the surface of a Ni anode during the OER is terminated with a NiO_2 layer. This finding contradicts the prevailing view that the active surface contains NiOOH. Nevertheless, the experimental Raman spectrum shows additional bands that were previously attributed to superoxide formation, which can only be rationalized by overtone and combination bands from the fundamental modes of NiO_2. Possible reasons for the appearance of these bands are discussed on the basis of additional Raman spectroscopy measurements on Co- and Mn-based oxides. Furthermore, variations in these bands caused by changing the pH, total ion concentration and applied potential might be incorrectly attributed to structural changes or the appearance of intermediates in the reaction mechanism[26,27]. Instead, we illustrate that these changes can be attributed to the vibrational Stark effect. We further discuss the implications of these findings for the interpretation of the OER mechanism. In summary, we show that the assignment of these bands to specific species, rather than overtones, could lead to misinterpretations of the material's structure and reaction mechanisms.

Results

Potential and electrolyte-dependent SER spectra

A cyclic voltammogram for the surface-enhanced Raman (SER) spectroscopy sample recorded in stirred 0.01 M KOH at a scan rate of 5 mV s^{-1} is shown in Fig. 1a, featuring typical redox features for Ni electrodes in this potential region[14,28]. A detailed description of the materials used, the experimental setup, the experimental procedures and the data evaluation can be found in the Methods and the Supplementary Methods. During the positive-going scan, a slight increase in current density is observed in the potential range between 1.1 and approximately 1.3 V_{RHE} (Volt vs. the reversible hydrogen electrode), which is not directly relevant to the present work; readers interested in further details should refer to the Supplementary Methods.

For potentials more positive than 1.3 V_{RHE}, $Ni(OH)_2$ is suggested to be oxidized to NiOOH in the oxidation peak O, with a maximum at about 1.49 V_{RHE}. The reverse reaction occurs in the reduction peak R with a maximum at about 1.2 V_{RHE} in the negative-going scan[26,27,29].

The change in the structural properties during the oxidation in peak O is apparent from in situ SER spectra in Fig. 1b, recorded at electrode potentials of 1.14 V_{RHE} (blue) and 1.54 V_{RHE} (black) (also marked in Fig. 1a by vertical lines). Further SER spectra recorded in steps of 0.1 V_{RHE} between these limits are included in Supplementary Fig. 4.

The SER spectrum for $Ni(OH)_2$ is similar to those reported previously, containing three distinct peaks in region A at 326 cm^{-1} (peak A_1), 456 cm^{-1} (peak A_2) and 501 cm^{-1} (peak A_3)[19,26,27,30,31]. The modes at 456 and 501 cm^{-1} were assigned to E_g or A_{1g} representations of the corresponding point group D_{3d}, while the mode at 326 cm^{-1} was assigned to the E_g irreducible representation[19]. Previous studies have shown that peak A_3 vanishes in crystalline samples and may be associated with hydrogen vacancies[30,31]. Additional bands appear between 850 cm^{-1} and 1,100 cm^{-1} (region B) and between 1,200 cm^{-1} and 1,500 cm^{-1} (region C). Region B has been observed both in situ and under ambient conditions (and high pressure)[27,32]. In the latter case, the band was assigned to an E_g mode[32]. Region C has, to the best of our knowledge, not been reported before. Finally, the feature at 1,650 cm^{-1} corresponds to the bending vibration of water[33].

When the electrode potential is increased to 1.54 V_{RHE} (around the onset of the OER), the SER spectrum changes substantially, as reported in numerous previous studies[19,26,27,29,34–39]. Possible changes at higher potentials will be discussed further below. In region I, the peaks A_1 to A_3 assigned to $Ni(OH)_2$ before the oxidation peak O disappear upon increasing the potential, and two intense modes at 479 and 560 cm^{-1}, denoted as I_1 and I_2, emerge. Studies aiming to assign these peaks are scarce. Mostly, these are related to Ni–O or Ni–OH moieties of NiOOH[26,39]. Similar peaks have been observed for both β- and γ-NiOOH[27,29,38]. Additional measurements reveal no discernible differences in the SER spectra of β- and γ-NiOOH (see Supplementary Note 1

https://doi.org/10.1038/s41929-026-01613-9

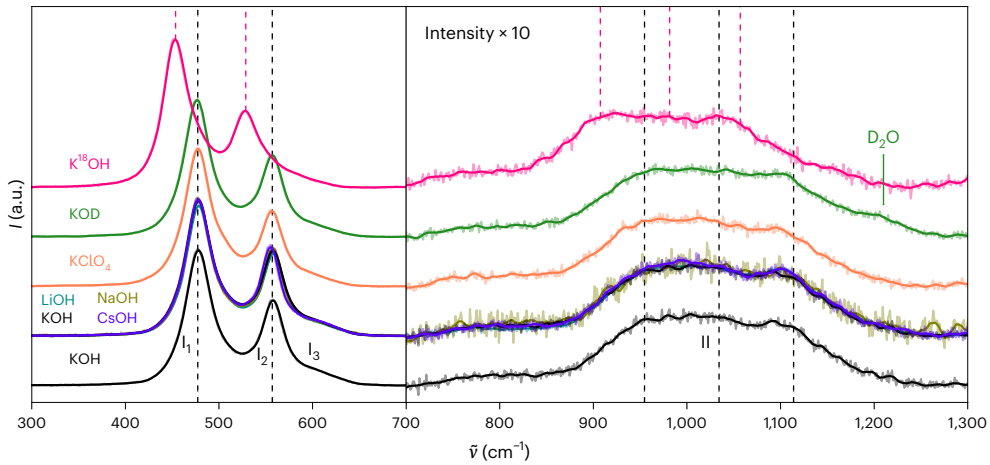

Fig. 2 | Surface-enhanced Raman spectra of oxidized Ni films on a Au wire in different electrolytes. In situ surface-enhanced Raman spectra of NiOOH recorded in 0.01 M KOH, LiOH, NaOH, CsOH, $KClO_4$ (pH 8.5), KOD and $K^{18}OH$ with an applied potential of 1.64 V_{RHE} without stirring. A waterfall plot of the spectra for the different cations is provided in Supplementary Fig. 8. The intensity scale is increased by a factor of 10 above 700 cm^{-1}. The four main features of NiOOH at 479, 560, 610 and 900–1,200 cm^{-1} measured in 0.01 M KOH are labelled as I_1, I_2, I_3 and II. Features I_1 and I_2 measured in KOH are marked in dashed black lines. Features I_1 and I_2 measured in $K^{18}OH$ are marked with dashed magenta lines. Overtones for KOH (black) and $K^{18}OH$ (magenta) are calculated using the features I_1 and I_2 from KOH and added to region II. The peak positions of I_1 and I_2 in all electrolytes are listed in Supplementary Table 5. Measurements in KOD include the D_2O bending vibrations at 1,210 cm^{-1}.

and 'Differences between surface and bulk structure' section). Hence, in the following, we simply refer to NiOOH.

A shoulder at 610 cm^{-1} (peak I_3) has been observed previously, but an explanation for its origin is still missing[26,27,29,34–37]. Additional bands appear at wavenumbers larger than 700 cm^{-1}, which we separate into two regions, that is, region II from 900 cm^{-1} to 1,200 cm^{-1} and region III from 1,400 cm^{-1} to 1,800 cm^{-1}.

Region II has been vividly discussed previously, especially with respect to possible reaction intermediates during alkaline OER[26,27,37,40]. It was concluded that the region consists of several convoluted peaks, which are possibly related to Ni superoxides ($Ni–OO^-$)[26,27], which is discussed in more detail below. Finally, region III from 1,400 cm^{-1} to 1,800 cm^{-1} has not been observed previously. The peak at 1,650 cm^{-1} likewise corresponds to the water bending vibration[33], which can be substantiated by additional measurements in KOD (Supplementary Note 2).

Ambiguous assignment of Raman peaks in the literature can be explained by the fact that SERS measurements carried out by different groups are generally conducted under dissimilar experimental conditions, such as sample preparation, choice and structure of the SERS substrate, electrolytes used and the excitation laser employed (wavelength and power). To mitigate related issues and to summarize recent results, we recorded in situ SER spectra for Ni deposited on roughened Au substrates (Au@Ni) electrodes at 1.64 V_{RHE} in different commonly used electrolytes (Fig. 2). Specifically, measurements were performed using 0.01 M KOH (black), LiOH (light blue), NaOH (olive), CsOH (violet), $KClO_4$ (orange), KOD (green) and $K^{18}OH$ (pink), where region I and region II are separated in Fig. 2a,b. The peaks in region I and II are almost identical upon changing the electrolyte from KOH to LiOH, NaOH or CsOH, indicating that these peaks do not depend on the cation type at a concentration of 0.01 M. Only the measurement in CsOH shows a small shift of about 2 cm^{-1} for the I_2 mode (Supplementary Note 3). For similar measurements performed in 0.1 M solutions, it was shown that the peak size and position can vary[36]. Moreover, several studies also show a shift for Cs^+ of about 0 to 5 cm^{-1} with respect to the other cations[27,36,41]. Some authors reported changes in region II and have attributed these variations to interactions between proposed superoxide species and alkali metal cations[36].

Using 0.01 M $KClO_4$ (pH 8.5, orange spectrum), and hence keeping the total ion concentration in the solution constant with respect to the 0.01 M KOH solution (pH 12, black spectrum), did not reveal any measurable changes in the peak position of either region I or II. Faint changes were only observed in the intensity of peak I_2. This result suggests that the structures probed by Raman are independent of pH, in contrast to previous reports[26,39]. Note that possible dissolution processes that could occur when changing the pH cannot be resolved with Raman, because the removal of parts of the oxide will not change the chemical composition of the probed layers. Small variations in the peak positions and intensities by changing the pH, together with the total ion concentration, are discussed further below in the context of the vibrational Stark effect. Furthermore, note that a commonly observed peak at 930–950 cm^{-1} related to ClO_4^- (ref. 42) is not observed in the SER spectra owing to its low concentration (Supplementary Note 4).

The possible presence of hydrogen atoms in the NiOOH structure is elucidated through measurements using isotope-labelled water. The SER spectrum recorded in KOD (black), when compared with that recorded in KOH (green), does not reveal any measurable changes, except for a small shoulder at around 1,210 cm^{-1} in KOD, which can be attributed to the D_2O bending vibration[33]. Similar results have been reported previously[27], suggesting that hydrogen is absent[38]. The absence of H in NiOOH has also been indicated by UV–Vis reflectance spectroscopy studies[43]. In turn, other studies using infrared spectroscopy and inelastic neutron scattering revealed the formation of hydrogen-bonded hydroxyl groups in the bulk structure and further suggested that protons are delocalized[18,19,44,45]. Thus, the behaviour of protons in NiOOH is not yet fully understood.

Using labelled oxygen ($K^{18}OH$), the peaks I_1, I_2 and I_3 shift from 479, 560 and 610 cm^{-1} to lower wavenumbers, that is, 454, 529 and about 590 cm^{-1}. Also, region II shifts to lower wavenumbers compared with measurements in KOH, as reported previously[26,27].

In total, on the basis of the shifts observed in $K^{18}OH$ in region II and the suggested lack of hydrogen species (inferred from measurements in KOD), region II is commonly associated with peroxide or superoxide species, which have been discussed as active oxygen species during the OER[26,27,39]. However, because region II appears already before the onset of the OER, some authors argue that bands in this region must be related to lattice moieties instead of an active oxygen intermediate[27]. Moreover, region II consists of a rather broad band, which is somewhat unexpected for superoxides, which, for other systems, such as CeO_2 and Pt oxides, usually consist of fewer and sharper peaks[46]. Consequently,

https://doi.org/10.1038/s41929-026-01613-9

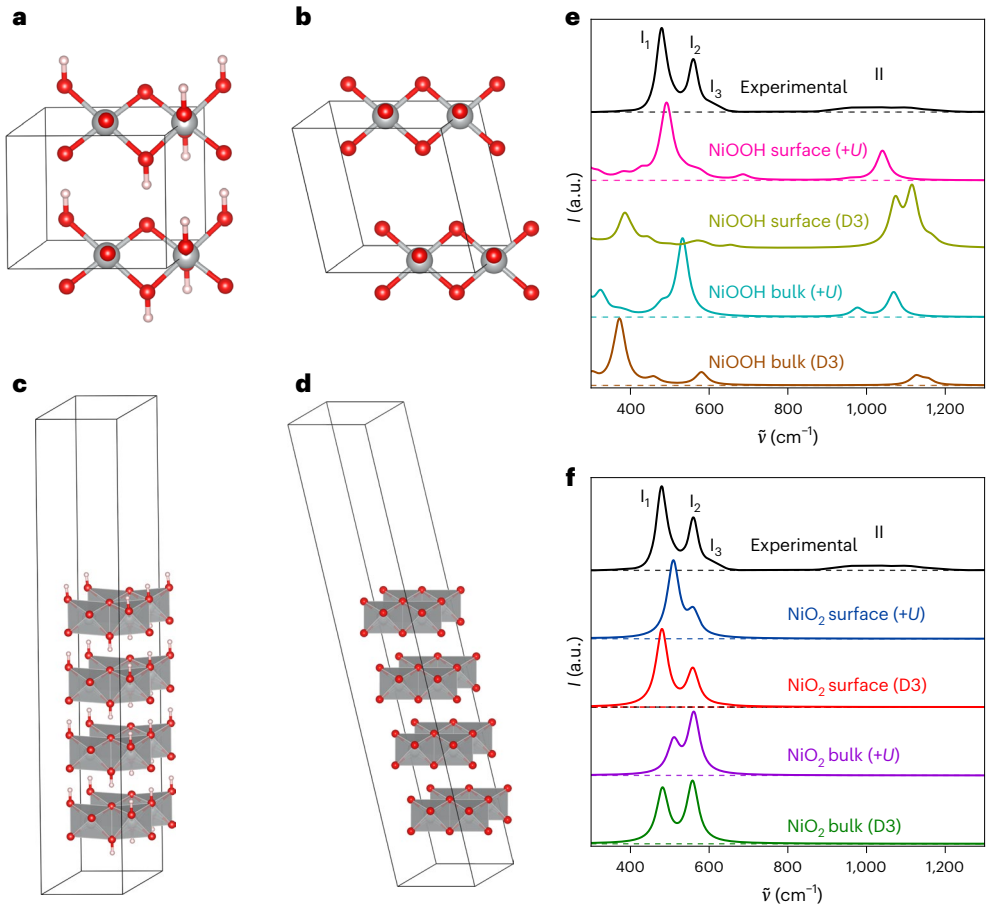

Fig. 3 | Density functional theory-computed structures and Raman spectra compared with experimental data. a–d, Relaxed geometries of NiOOH bulk (ferromagnetic) (**a**), NiO_2 bulk (**b**), NiOOH (ferromagnetic) (**c**) and NiO_2 (**d**) surface slabs calculated with D3 corrections. Ni atoms are shown in grey, O in red and H in white. **e**, Raman spectra of the NiOOH bulk and NiOOH surface calculated with either Hubbard-*U* (5.5) correction or D3 dispersion correction using a ferromagnetic low-spin configuration. Calculations with antiferromagnetic spin configurations are shown in Supplementary Fig. 10. **f**, Raman spectra of NiO_2 bulk and NiO_2 surface calculated with either Hubbard-*U* (5.5) correction or D3 dispersion correction. Calculated spectra are displayed using an arbitrary Lorentzian peak width for comparison with experimental data. Experimental SER spectra in 0.01 M KOH at 1.54 V_{RHE} measured without stirring are also shown in **e** and **f**.

the precise origin of region II remains unclear on the basis of current understanding of Raman spectra.

DFT-guided assignment of Raman spectra

The peaks I_1, I_2 and I_3 in the experimental SER spectra of NiOOH have not yet been unambiguously assigned to a specific surface structure. Nevertheless, a substantial number of theoretical studies report on various properties of NiOOH, predominantly focussing on the structure of NiOOH at the onset or during the OER[15,47,48]. However, none of the theoretical studies explicitly show computed Raman spectra. Hence, a direct correlation between experiment and theory has not been established.

To approach this gap in the literature, we computed SER spectra for various bulk and surface structures using periodic DFT calculations with the Vienna ab initio Simulation Package. Detailed information on the calculations, considered structures and the calculated Raman spectra can be found in the Methods.

To interpret the experimentally measured SER spectra, we considered four structures in our computational study, that is, NiOOH and NiO_2 bulk systems, as well as a (0001) surface for each of these Ni (hydr)oxides (Fig. 3). On the basis of previous studies[15,20], we adopted a brucite-type structure for bulk β-NiOOH (Fig. 3a), which is similar to that of $Ni(OH)_2$ with half of the hydrogen atoms removed. We further consider an ABBCCA O-layer stacking order, as suggested by theory[15]. Additionally, all NiOOH structures were calculated with both ferromagnetic and antiferromagnetic spin configuration, which does not seem to have a substantial influence on the computed Raman spectra (Supplementary Fig. 10). In the following, we only show spectra for the ferromagnetic configuration. For the bulk NiO_2 structure, the H atoms of bulk β-NiOOH were removed and the structure was relaxed. As a result, the ABBCCA O-layer stacking order transformed into an ABAB stacking order. Finally, surface structures for both NiOOH and NiO_2 were calculated with vacuum, resulting in a layer-to-layer distance of around 18 Å. The corresponding calculated Raman spectra for all structures (excluding the antiferromagnetic configuration) are shown in Fig. 3, including the experimental data (black curve) for reference. The full spectra for both NiOOH structures, including the antiferromagnetic configuration, with additional modes below 300 and above 1,300 cm^{-1}, are shown in Supplementary Fig. 10.

We first focus on the computed Raman spectra of the NiOOH structures in Fig. 3e. For the bulk structure of β-NiOOH (brown and light blue, using D3 or Hubbard correction, respectively), several peaks are observed below 600 cm^{-1} and insufficiently fit the fundamental modes observed in the experiment. Furthermore, OH bending vibrations are observed between 900 and 1,200 cm^{-1}, which roughly match the position of region II. Finally, OH stretching vibrations are predicted (Supplementary Fig. 10) but not observed in the experiment. Raman spectra of the surface structures show a similar behaviour, with peaks having different intensities that are shifted with respect to the

https://doi.org/10.1038/s41929-026-01613-9

Table 1 | Calculated peak positions for NiO_2

Method	Peaks and point groups			
	I_1	—	I_2	I_3
	E_g	E_u	A_{1g}	A_{2u}
Experimental	479	-	560	610[a]
Bulk (+D3)	481	553	558	631
Bulk (+*U*)	508	556	561	650
Surface (+D3)	479	556	559	638
Surface (+*U*)	508	556	560	653

The values are DFT-calculated positions for vibrational modes of NiO_2 (point group D_{3d}). E_g and A_{1g} are Raman-active (but IR-inactive) modes, while E_u and A_{2u} are IR-active (but Raman-inactive) modes. Experimental peak positions are added for comparison. [a]The position of peak I_3 can only be determined approximately, as it does not form a distinct peak.

peaks of the bulk Raman spectrum. Overall, none of the calculations could reproduce region I as observed in the experiment. In addition, because the isotope-labelled experiments did not show any shift with deuterium in the SER spectrum, the DFT-calculated structures containing hydroxyl groups might not correspond to those captured by the experiment.

A potential hydrogen-free structure is NiO_2, whose structure is based on deprotonated $Ni(OH)_2$. The corresponding computed Raman spectra for NiO_2 bulk (green with D3, violet with DFT+*U*) and surface (red with D3, blue with DFT+*U*) are shown in Fig. 3f, including the experimental Raman spectrum (black). The position of the modes and their representations are summarized in Table 1 along with the experimental peak positions.

Independent from the computational approach (D3 or +*U*) and the structure (bulk or surface), two Raman active modes are predicted, closely matching the positions of the peaks I_1 and I_2 observed in the experiment. For the surface structures, the intensities of the peaks match those in the experiment (inverse intensity ratios are found for the bulk structures). Peaks in region II are missing in all calculations, and no further peaks are observed outside of the range of wavenumbers presented in Fig. 3f. Even though peak I_3 is not reproduced in the computed Raman spectrum, the calculations show a Raman-inactive A_{2u} mode (surface and bulk) that aligns closely with peak I_3 of the experimental Raman spectrum (Table 1), suggesting that the two peaks might be related. Furthermore, the calculations also suggest a Raman-inactive E_u mode, located between peaks I_1 and I_2.

In principle, distortions of symmetry of the structure can disrupt vibrational modes[49,50], such as E_u and A_{2u}. Consequently, these selection rules are lifted, allowing both modes to become Raman active. Such distortions can be particularly pronounced at the surface, especially in the presence of an electric field, as discussed below in the context of the vibrational Stark effect.

To further rationalize that the experimental Raman spectrum corresponds to NiO_2 rather than NiOOH, we compared the calculated density of states and structural properties of both systems with experimental and computational results. The former turns out to be non-conclusive because band gaps inferred from reported experimental values[51,52] show large variations. Given these discrepancies, a more detailed discussion of the density of states is provided in Supplementary Note 7.

More conclusive answers can be drawn by comparing the interatomic distances of Ni–Ni and Ni–O for the calculated structures (this work) and reported experimental results, summarized in Table 2. The DFT-computed interatomic distances for the individual computational methods are expanded in Supplementary Table 3.

Overall, good agreement between computational and experimental data is observed for both NiO_2 and $Ni(OH)_2$. More specifically, for NiO_2, the calculated interatomic distances are consistent with reported extended X-ray absorption fine structure (EXAFS) measurements and

Table 2 | Experimental and computed interatomic distances for various Ni (hydr)oxides

Structure	Method	Ni–Ni distance (Å)	Ni–O distance (Å)	Ref.
NiO_2	Theory	2.77–2.82	1.85–1.88	This work
NiOOH	Theory	2.87–2.99	1.86–2.11	This work
$Ni(OH)_2$	Theory	3.12–3.23	2.07–2.11	This work
NiO_2	EXAFS	2.82	1.88	53
$Li_{0.03}NiO_2$	EXAFS	2.82	1.89	54
$Li_{0.01}NiO_2$	XRD	2.81–2.82	—	55
NiOOH	EXAFS	2.82 and 3.13	1.88 and 2.07	57
NiOOH	EXAFS	2.82–2.86 and 3.09	1.88–1.92 and 2.12	22
NiOOH	EXAFS	2.82	1.86	58
NiOOH	EXAFS	2.83–2.84	1.89–1.92	61
NiOOH	EXAFS	2.84	1.89	62
NiOOH	EXAFS	2.82	1.88	63
NiOOH	EXAFS	2.81	1.85	27
NiOOH	EXAFS	2.81	1.86	64
NiOOH	XRD	2.82	—	20
$Ni(OH)_2$	EXAFS	2.82 and 3.13	2.05	57
$Ni(OH)_2$	EXAFS	3.11	2.05	58
$Ni(OH)_2$	EXAFS	3.11	2.08	27
$Ni(OH)_2$	XRD	3.07	—	20

'Theory' refers to interatomic distances inferred from the DFT-computed structures of $Ni(OH)_2$, NiOOH and NiO_2 using PBE+D3, PBE+U, PBE0, B3LYP and HSE06 functionals. Experimental values are inferred from the literature from the given sources and are based on extended X-ray absorption fine structure (EXAFS) and X-ray diffraction (XRD) measurements. More extensive results for calculated interatomic distances, split into the individual methods, are given in Supplementary Table 3.

also previous computational studies[53–56]. This agreement is further supported by the work of Fantin et al., reporting on Raman spectra of $Li_{0.01}NiO_2$, assigned to Ni(IV) species (confirmed by hard X-ray photoelectron spectroscopy)[55], which closely resemble the Raman spectra in this work. Similarly, the calculated Ni–Ni and Ni–O distances for $Ni(OH)_2$ are in good agreement with experimental values[20,27,57,58] (only the calculated Ni–Ni distance obtained in this work using PBE+D3 is slightly overestimated at 3.23 Å).

For NiOOH, the interpretation is more complex. First, the calculated Ni–Ni distances for NiOOH span a wide range of values, attributed to a Jahn–Teller distortion, which has also been reported in previous computational works[15,16,47,48,59,60]. Second, some experimental works present two values[22,57], which were also rationalized by a Jahn–Teller distortion, although most studies report only a single distance (the shorter one)[20,27,58,61–64]. None of these reported experimental values match our computed interatomic distances for NiOOH. Interestingly, both reported experimental Ni–Ni distances of NiOOH match either that of NiO_2 (shorter distance) or that of $Ni(OH)_2$ (longer distance), as suggested by our calculation and previously reported measurements of NiO_2 (refs. 53–55) and $Ni(OH)_2$ (refs. 20,27,57,58). For the Ni–O distances, the assignment is less clear, because the values can be assigned to interatomic distances of experimental and theoretical values of either NiO_2 or $Ni(OH)_2$. However, the reported values also fit the largest and smallest values from our calculation on NiOOH. Note that some values in the range of the calculated values of NiOOH do not match any experimental values.

In general, we suggest that, on the basis of this comparison, it is likely that the NiOOH phase discussed in the literature might actually be a mixture of $Ni(OH)_2$ and NiO_2, which has also been suggested previously[63,65]. The possible role of mixed phases is further elaborated on in 'Differences between surface and bulk structure' section.

https://doi.org/10.1038/s41929-026-01613-9

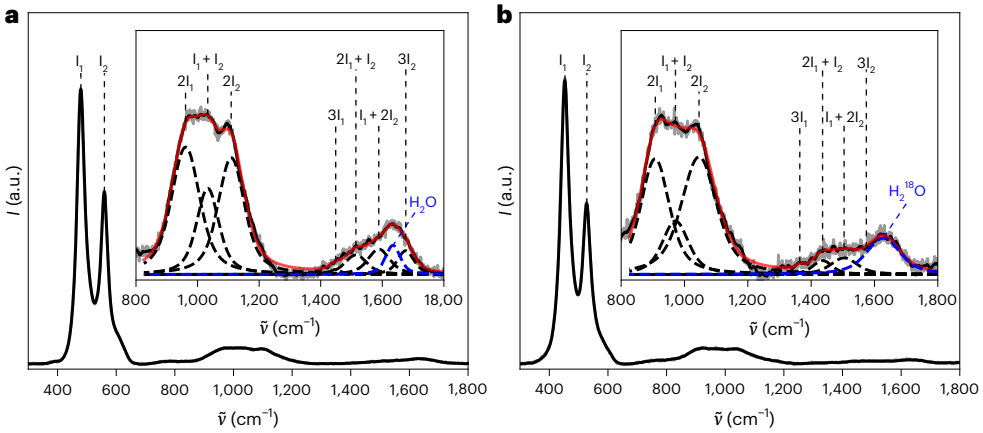

Fig. 4 | Overtone deconvolution of surface-enhanced Raman spectra of oxidized Ni in pure and labelled water. a,**b**, In situ surface-enhanced Raman spectra of NiO_2 on Au@Ni recorded at an applied potential of 1.54 V_{RHE} up to 1,800 cm^{-1} in 0.01 M KOH (**a**) and 0.01 M KOH (**b**) with $H_2^{18}O$ as solvent. The inset of both spectra highlights the first and second overtone and combination bands. The position of possible overtone, combination modes and the position of the $\nu_2(H_2O)$ bending vibration of water are highlighted. Using only the calculated position within a margin of ±10 cm^{-1} of the predicted peaks, the spectra in the inset were deconvoluted. Additionally, the deconvolution contained the H_2O or $H_2^{18}O$ bending vibration.

Furthermore, on the basis of the detailed comparison above (DFT and experimental interatomic distances) and the lack of a deuterium shift in our isotope-labelling experiments (Fig. 2), we now assign the Raman spectrum close to the OER to NiO_2 rather than NiOOH. Note that the computed Raman spectrum does not yet capture the peaks observed in region II, and neither of the other structural models provided insights on the origin of region III (Fig. 1b), which is the subject of the next section.

Overtone and combination band dormation in Raman spectra

An often-overlooked aspect in the interpretation of Raman spectra is the role of overtones, also referred to as higher-order harmonics or higher-order scattering. In general, overtone and combination modes in Raman spectra would be forbidden according to the selection rules in the harmonic approximation. However, as described above (and below), under certain conditions, such features can appear[8]. Within the harmonic approximation, the positions of overtones correspond to integer multiples of fundamental modes, while combination modes result from the sum of different fundamental modes.

To discuss the role of overtones, we highlight region II and III of the experimentally measured SER spectrum of NiO_2 (formerly assigned to NiOOH) in Fig. 4a (inset) and indicate possible overtone and combination modes. The first overtones of peaks I_1 and I_2 are expected at twice the measured positions of the corresponding fundamental modes, that is, at $2I_1$ and $2I_2$, while the combination of both modes would appear at $I_1 + I_2$, as marked in the inset. These peaks are all within region II of the SER spectrum. Using the positions of these overtones and the combination band, we deconvoluted region II into three peaks (dashed curves in the inset of region II), where the sum of the peaks (red curve) follows the experimental Raman spectrum in this region. Details on the fitting procedure are provided in the Methods. The positions of the most relevant deconvoluted peaks for the discussion are summarized in Supplementary Table 6, including overtones in KOD (Supplementary Note 2) and $K^{18}OH$ (Fig. 4b).

Elaborating further on possible higher overtones, we suggest that region III (1,400–1,800 cm^{-1}) consists of the second-order overtones of the fundamental peaks I_1 and I_2 as well as the combination modes from these peaks. For the deconvolution, we also considered the band related to the bending mode of H_2O (marked in blue). In addition, combination bands with peak I_3 are expected to appear within the respective overtone regions. However, the intensity of peak I_3 is low, and a possible contribution to region II will be discussed with the potential-dependent measurements shown in 'Influence of the vibrational Stark effect' section and in Supplementary Note 8.

A similar peak deconvolution approach can be used for SER spectra recorded in KOD, where, in addition, the bending vibration related to D_2O at 1,200 cm^{-1} has to be taken into account, as demonstrated in Supplementary Note 2.

More interesting is the deconvoluted SER spectrum for NiO_2 recorded in $K^{18}OH$ (Fig. 4b). Here, the fundamental modes (peaks I_1 and I_2) shift to lower wavenumbers. Hence, the overtones and combination modes also shift to lower wavenumbers in regions II and III. The peak related to $H_2{}^{18}O$ at 1,628 cm^{-1} is considered in the deconvoluted SER spectrum. Consequently, previous studies claiming that this region II is associated with oxygen are, in principle, true. However, the shifts in regions II and III are only an indirect effect caused by the shift of the fundamental modes related to lattice oxygen species rather than shifts in the vibrational modes of reactive oxygen intermediates, which could be expected in this region II with pronounced peaks[46]. Note that, for some systems or conditions, such species could still appear and fall near or within overtone bands. Reliable assignment then requires bands that cannot be deconvoluted with the position of higher-order harmonics for at least one isotope.

In summary, assigning the bands in regions II and III to overtones and combination modes allows us to revisit the previously discussed DFT-calculated Raman spectra and rationalize their absence. Apparently, these modes arise from anharmonic effects, which are not accounted for by the finite difference approach that we employed to calculate phonon modes. Thus, with the origin of regions II and III accounted for, the DFT-calculated Raman spectrum of NiO_2 aligns well with the experimental findings, further supporting our suggestion that the Raman spectrum corresponds to that of NiO_2.

Further insights on the possible origin of the overtone and combination modes can be gained from comparing Raman measurements with and without SERS support and recorded at different potentials. First, overtones are also apparent in the in situ Raman spectra of Ni sheets oxidized to NiO_2 without SER support, measured under similar conditions, albeit with reduced intensity, as demonstrated in Supplementary Fig. 5. Therefore, it is unlikely that the observed overtones originate from a SERS effect. In contrast, a Raman spectrum for $Ni(OH)_2$ can only be observed in the presence of a SER substrate (Fig. 1b, blue curve). Here, the additional features B and C in the experimentally obtained SER spectrum can also be explained by overtones, as demonstrated in Supplementary Note 9.

https://doi.org/10.1038/s41929-026-01613-9

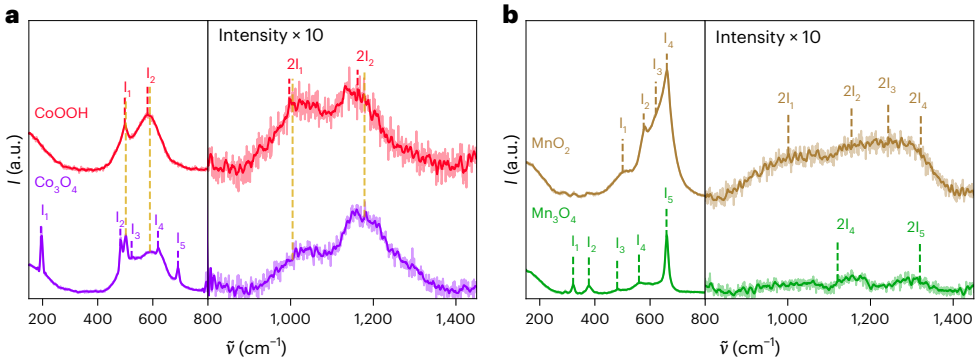

Fig. 5 | Surface-enhanced Raman spectra of a Au wire supported Co- and Mn-based oxides at different potentials. a, In situ SER spectra of Co deposited on Au wire in 0.01 M KOH at 0.77 V_{RHE} (violet; 194, 482, 523, 619 and 691 cm^{-1}) and 1.17 V_{RHE} (red; 498 and 581 cm^{-1}), where Co_3O_4 and CoOOH is formed, respectively. The fundamental modes of both Co_3O_4 and CoOOH are highlighted with a dashed line, including the modes of CoOOH contamination (yellow) in the spectrum of Co_3O_4. Additionally, the overtones of CoOOH of both materials are highlighted. **b**, In situ SER spectra of Mn deposited on Au wire in 0.01 M KOH at 0.67 V_{RHE} (green; 321, 378, 481, 560 and 660 cm^{-1}) and 1.47 V_{RHE} (brown; 501, 577, 621 and 661 cm^{-1}), where Mn_3O_4 (and Mn_2O_3) and MnO_2 is formed, respectively. The fundamental modes are marked, and the respective overtones of MnO_2 and possible overtones of I_4 and I_5 of Mn_3O_4 are highlighted. The assignment of Raman spectra was performed on the basis of previous literature summarized in Supplementary Table 8.

The most common possible reasons for the appearance of overtones would be related to the resonance-enhancement effect, which was previously proposed for NiOOH for excitation at a laser wavelength of 633 nm (refs. 26,35). In contrast, no resonance effect is known or stands out for $Ni(OH)_2$ at this wavelength. While the first overtones can occur owing to resonance Raman scattering in the form of triple-resonance Raman scattering, the occurrence of a complete second overtone band is unlikely owing to selection rules[8–10].

Hence, resonance enhancement alone does not fully rationalize the observed overtone features in our case.

Considering reports on overtones and combination modes for other systems, it seems that these features appear predominantly in layered materials such as MoS_2 (ref. 10). Other examples of overtones in layered materials are summarized in Supplementary Table 7. Additionally, some rare examples report overtones for non-layered materials, such as RuO_2 powder[66]. For some but not all of these systems, overtone and combination modes were also suggested to be related to resonance effects[10].

To substantiate our assumption that layered materials predominantly show pronounced overtones, we additionally recorded in situ SER spectra of Co and Mn in 0.01 M KOH at two potentials (Fig. 5). The peaks commonly reported in the literature are marked in the spectra. The band positions and the surface structures to which they have been assigned are given in Supplementary Table 8, including references. For Co, at 0.77 V_{RHE} (purple), the electrode consists of a mixture between Co_3O_4 and CoOOH. At 1.17 V_{RHE} (red), presumably only CoOOH is present.

Most importantly, CoOOH is considered to have a layered structure, while Co_3O_4 has a rigid spinel structure. According to our assumption, for CoOOH (red), the peaks in region II are related to overtone and fundamental modes. For the SER spectrum of Co_3O_4 (violet), we suggest that the overtone region is dominated by the overtones from CoOOH, because the shape does not change substantially and also no additional features that could be attributed to overtones of the fundamental modes of Co_3O_4 appear in region II.

Comparable conclusions can be drawn from the Raman spectra of Mn shown in Fig. 5b. At 0.67 V_{RHE}, the five bands in the SER spectrum can be attributed to Mn_3O_4, although Mn_2O_3 might as well be present. Both Mn_3O_4 and Mn_2O_3 possess a rigid structure. The overtone region only shows two weak features that may vaguely correspond to the overtones of I_4 and I_5 of Mn_3O_4. Admittedly, the intensity of the fundamental modes is low for Mn_3O_4, which may result in potential overtone bands being obscured by noise. Upon applying 1.47 V_{RHE}, the Raman spectrum changes markedly. According to previous reports, the features can be attributed to MnO_2, but they probably reflect a mixture of MnO_2 phases, including layered structures with intercalated cations. Also, in this case, the overtone region matches the overtones of the fundamental peaks.

Overall, the measurements of Co, Mn and Ni substantiate a tendency for layered materials to exhibit overtone modes. In general, these materials are prone to defects and mismatches due to comparably weak interlayer interactions[67]. Therefore, we suggest that the overtones might be enhanced or even induced by such defects or intermolecular interactions between the layers. This appearance of overtones could potentially aid in discriminating between layered phases and more rigid, non-layered structures, such as in CoOOH and Co_3O_4. Note that these findings do not indicate that overtones occur only in layered materials, which is further supported by the possible weak overtone features detected for Mn_3O_4 or the previously reported overtones in RuO_2 powders[66]. Further studies are required to elaborate on these aspects more closely.

Influence of the vibrational Stark effect

So far, our results and discussion on the Ni oxide structure focussed on the potential region before and at around the onset of the OER. Below, we illustrate the consequences of assigning the peak in region II to overtones on the interpretation of SER spectra recorded during the OER, by performing in situ SERS measurements on Au@Ni electrodes in 0.01 M KOH with increasing potential and varying ion concentration (Fig. 6).

The evolution of the Raman spectra with increasing potential (from 1.54 to 2.74 V_{RHE}) in 0.01 M KOH are shown in Fig. 6 (see Supplementary Fig. 12 for an overlay plot). Focussing on region I, peak I_1 shifts slightly to higher wavenumbers and the intensity of peak I_2 increases, as does that of peak I_3, which also shifts slightly to higher wavenumbers (6–10 cm^{-1}). Furthermore, subtle changes can be observed between peaks I_1 and I_2, which may be associated with potential-dependent changes in the E_u band (see below and Supplementary Note 8). Whether or not these shifts originate from the presence of adsorbed species cannot be excluded from our work. However, usually, adsorbed species (such as O or OH) should lead to the appearance of additional sharper bands at higher wavenumbers[46]. The formation of an adsorption complex would then possibly also lead to a substantial change in the vibrational properties of the fundamental modes. In region II, the changes observed are more complex, developing two broad features.

The pronounced changes at high wavenumbers of the overtone and combination band in region II can be rationalized by the changes

https://doi.org/10.1038/s41929-026-01613-9

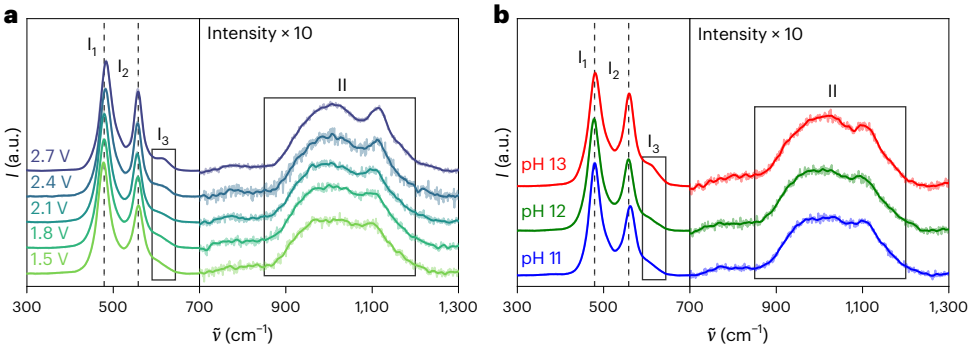

Fig. 6 | Vibrational Stark effect in surface-enhanced Raman spectra of NiO_2. a, In situ surface-enhanced Raman spectra of NiO_2 on Au@Ni from 1.54 to 2.74 V_{RHE} recorded in 0.01 M KOH. **b**, In situ surface-enhanced Raman spectra recorded in 0.1 M, 0.01 M and 0.001 M KOH at 1.6, 1.64 and 1.58 V_{RHE}. All measurements were performed while stirring to prevent bubble formation. Region I (I_1, I_2, I_3) and II are marked, and modes where changes are visible are highlighted. The data in region II from 700 to 1,250 cm^{-1} is scaled by a factor of 10.

in peak shape, intensity and position of the fundamental modes in region I. Furthermore, the influences of peak I_3 on the overtone band can be observed at high potentials (Supplementary Fig. 12), indicating that it corresponds to a fundamental mode of the lattice, in agreement with our earlier assignment of this peak I_3 to the IR-active A_{2u} mode on the basis of DFT calculations. This also means that these modes are present at lower potentials but only become discernible by changing the potential. The extent to which the second possible IR-active E_u mode inferred from DFT above contributes to the overtone region is unclear. The findings underscore that potential-dependent measurements can indirectly reveal modes through changes in the fundamental and overtone regions.

The peak changes and shifts observed upon varying the potential can also be induced by using electrolytes with varying pH (and varying total ion concentration), such as 0.1 M, 0.01 M and 0.001 M KOH, while applying a potential of 1.60 V_{RHE}, 1.64 V_{RHE} and 1.58 V_{RHE}, as illustrated in Fig. 6b. In the case that the total ion concentration is kept constant upon varying the pH, the SERS bands remain unchanged, as illustrated in Fig. 2.

In combination, on the basis of these measurements, we suggest that the changes in the vibrational properties observed in the Raman bands are related to changes in the interfacial electric field at the electrode surface, denoted as the vibrational Stark effect[68]. Upon applying a potential to the electrode, the field in the double layer will simply follow. Similarly, changing the ion concentration (and in this case, also pH) in the solution will change the local accumulation of ions close to the electrode and hence cause a change in the interfacial electric field. Keeping the ion concentration constant upon changing the pH (Fig. 2), the interfacial electric field does not change and hence the Raman spectra appear similar. Note that the local electric field also depends on the nature of the ions. This influence probably accounts for the small shift observed for Cs^+ compared with Li^+, Na^+ and K^+ in Fig. 2 and might become more pronounced in more concentrated solutions.

Such Stark effects have previously been observed in SERS studies of adsorbed species such as CO on Pt, affecting both the position (by up to 5.3 cm^{-1} per 0.1 V_{RHE} step) and the intensity of the vibrational modes[69]. Considering these findings and our results, we suggest that the Stark effect contributes substantially to the changes observed in both the fundamental modes and the overtone regions II and III. Consequently, possible structural modifications or the presence of adsorbed species, as well as the associated OER mechanisms that were attributed on the basis of changes in this region, might have to be reconsidered[26,27,39].

Differences between surface and bulk structure

Considering that our combined Raman and DFT study suggests that, after the electrochemical oxidation of $Ni(OH)_2$ (oxidation state II), NiO_2 (oxidation state IV) is formed at the surface instead of the widely accepted NiOOH (oxidation state 3.0), and the discrepancies between the various structural models highlighted throughout this work, we briefly discuss possible surface, near-surface and bulk structures at high overpotentials in alkaline electrolytes (OER region). An impression about the relative stability of the potential- and pH-dependent stability of these phases can be inferred from experimental and computational Pourbaix diagrams[23–25]. Some studies predict the direct formation of NiO_2 from $Ni(OH)_2$ without the formation of a stable NiOOH intermediate, while others identify a narrow stability window for NiOOH. Most importantly, all reports agree that NiO_2 becomes the thermodynamically favoured phase at high pH and high potential.

While this conclusion supports our findings, it conflicts with other studies reporting oxidation states for chemically prepared β- and γ-NiOOH ranging from 3.0 to 3.7, as determined by titration[14,20,70], or bulk-sensitive X-ray absorption near edge structure (XANES) measurements of electrochemically oxidized samples reporting mixed oxidation states between 3.22 and 3.6 (refs. 22,27,58,61,62,71–73). Although these measurements suggest or confirm the presence of Ni(IV), they also suggest lower oxidation states, typically attributed to hydroxide species, which were not detected in the Raman spectra, on the basis of isotope-labelled experiments in D_2O. Experimental methods that permit resolution of the catalyst surface structural properties under reaction conditions beyond Raman spectroscopy remain scarce, especially because Ni oxides with high oxidation states tend to decompose when removed from the electrolyte for ex situ characterization, such as X-ray photoelectron spectroscopy (XPS)[70,74]. Thus, synchrotron-based techniques such as EXAFS measurements on thin films are among the few methods capable of providing in operando structural insights. Along that line, some EXAFS studies have suggested the direct oxidation of Ni(II) to Ni(IV) instead of Ni(III) by analysing interatomic distances[63,65]. Similar conclusions were drawn in 'DFT-guided assignment of Raman spectra' section. However, other authors have also suggested mixed oxidation states including Ni(III) using XANES[22,27,58,71,72]. Detection of hydrogen in bulk-sensitive inelastic neutron scattering[19] and infrared spectroscopy[18,44,45], revealing hydrogen-bonded hydroxyl groups, further supports the presence of NiOOH but could also support a mixture of NiO_2 and $Ni(OH)_2$. Overall, we suggest that the apparent discrepancies in structural assignment arise from the different probing depths of the employed techniques. Methods such as EXAFS and X-ray diffraction usually provide combined information about the surface as well as the bulk and thus also very much depend on the nature of the sample, such as thin-film thickness or particle sizes, and the choice of the support. For SERS, the question about the probing depth cannot be answered with as much confidence, because to the best of our knowledge, dedicated studies on the probing depth of Raman on solid materials are

not available. Possible hints about the probing depth of the substrate can be gained indirectly from Raman studies. For example, in studies without electrolyte and without SERS substrate, a Raman scattering study on MoS_2 layers supported on SiO_2 showed that the Si signal from the substrate decreases with increasing MoS_2 layer thickness, vanishing entirely for more than five layers[10]. In a much more related system, but also without a SERS substrate, Li_xNiO_2, the Raman probing depth has been suggested to range from 100 to 200 nm (ref. 55). For solids in electrolytes and using SERS substrates, a probing depth of 3–4 nm was suggested in SERS measurements on the electrooxidation of Cu on a Au substrate[75]. We used a similar approach, and by analysing the time-dependent evolution of the SER spectra during Ni electrooxidation to $Ni(OH)_2$, we obtain a probing depth smaller than 3.2 nm, that is, less than seven monolayers (Supplementary Note 10). These insights suggest that the probing depth strongly depends on the experimental conditions and the material.

Consistent with this picture, no new features appear in the Raman spectra after continuous oxidation at 1.49 V_{RHE} or at higher potentials (up to 2.7 V_{RHE}; Figs. 1a and 6b). Such changes in bulk structure are apparent in cyclic voltammagrams when a Ni electrode is exposed to extended oxidation reduction cycles to form β- and γ-NiOOH (Supplementary Note 1). Because the Raman spectra remain unchanged (NiO_2), these structural changes must occur in the bulk, which is not accessible with SERS. Consequently, the bulk composition, whether NiOOH or a mixture of NiO_2 and $Ni(OH)_2$ (see 'DFT-guided assignment of Raman spectra' section), cannot be conclusively determined with our methodology. This also means that changes in the bulk structure seem to have little effect on the surface structural properties of the terminating NiO_2 layer, thus possible effects on electrocatalytic reactions might be negligible.

Mechanistic implications

Our revised identification of the surface structure (NiO_2 versus NiOOH) and the fact that SERS does not provide direct evidence of reaction intermediates will probably have consequences for current endeavours to understand the still-unresolved OER mechanism on Ni anodes. In general, for the previously suggested NiOOH(0001) surface, several mechanisms were suggested[16,76,77]. Usually, two mechanisms are primarily discussed to describe the OER: the lattice oxygen mechanism (LOM), in which lattice oxygen directly participates in the reaction, and the adsorbate evolution mechanism (AEM), where all evolved oxygen originates from the electrolyte[78]. For both mechanisms for NiOOH, a favourable suggested first step is the deprotonation of lattice OH groups, followed by the adsorption of H_2O or OH^- at the resulting deprotonated site[16,77]. Considering now that NiO_2 provides the active sites, such a deprotonation step could be discarded from the catalytic cycle.

In an AEM in subsequent steps, after the adsorption and deprotonation of H_2O or OH^-, either the deprotonated species react with another H_2O or OH^- from the electrolyte or two of these adsorbed deprotonated species recombine to form O_2, recovering the NiO_2 surface. Considering that the O–O distance (Table 2) of NiO_2 (2.77–2.82 Å) is shorter compared with NiOOH (2.87–2.99 Å), and hence that of adsorbed oxygen atoms also is, the recombination to form O_2 would be facilitated. However, the distance between neighbouring adsorbed oxygen species still remains relatively large, compared with other materials, such as IrO_2 where Ir–O_4–Ir coupling was suggested, allowing direct bonding between adsorbed O[79].

The LOM would only require the formation of a single deprotonated OH^- or H_2O on a lattice oxygen atom, which is released with the lattice oxygen of the adsorption site. The thereby created vacancy would be filled by adsorption and deprotonation of OH^- or H_2O in the final step. The involvement of the lattice oxygen species was demonstrated by ^{18}O isotope-labelling experiments[37,80]. Furthermore, DFT-based mechanistic studies on NiO_2 derived from deprotonated isolated two-dimensional NiOOH sheets, that is, where the lattice constant is not that of a pure NiO_2 structure, support a LOM mechanism and ascribe the NiO_2 structure a lower overpotential for the OER than NiOOH[81].

Finally, one has to consider that real catalyst materials, including the system studied in this work, consist of edge and defect sites as well as grain boundaries, which are difficult to isolate experimentally. For NiO_2, it is likely that these sites behave differently from those on NiOOH[81]. Similar extensive theoretical studies to those on NiOOH-[62,77,80] and NiO_2-like structures[81] are now required for NiO_2; aside from the structural effects, they should also consider the possible influence of the oxidation state, the magnetization and geometry on the OER.

Conclusion

In this Article, we highlight the implications of overtone formation, in combination with isotope-labelled experiments and DFT-computed Raman spectra, for surface structural assignment, as demonstrated by the oxidation of Ni in alkaline electrolytes at potentials near and beyond the onset of the OER using SERS. The surface structural properties were elucidated by combining experiments in isotope-labelled water with DFT-computed Raman spectra. These combined findings, including the absence of a deuterium shift (isotope-labelled experiments) in the experimental Raman spectra, illustrate that the surface is terminated by Ni(IV)O_2 rather than the widely discussed Ni(III)OOH. Next, we attribute the experimentally observed Raman bands of NiO_2 between 900 cm^{-1} and 1,200 cm^{-1}, previously assigned to superoxides, to overtones and combination bands. This assignment is further substantiated by the detection of second-order overtones in the SER spectra of NiO_2, as well as both first- and second-order overtones in the SER spectra of $Ni(OH)_2$. We propose that layered materials are particularly prone to exhibiting overtones, which was substantiated by additional potential-dependent Raman measurements on Co- and Mn-based oxides and should stimulate further fundamental Raman studies on this class of materials.

In addition, we show that, according to the SERS data, the surface structure of NiO_2 in an alkaline environment is not directly affected by pH, the type of cation such as Li^+, Na^+, K^+ and Cs^+ or possible phase transitions between β- and γ-NiOOH in the bulk. Moreover, we rationalized the changes observed in the SER spectra in the overtone region at increasing potentials or increasing electrolyte concentration, previously assigned to structural changes of the material, to a vibrational Stark effect.

We believe that these findings are relevant to the ongoing discussion of the structure and understanding of the catalytic behaviour of oxides, in particular for the reaction mechanism of the OER. Moreover, the observation of overtones for different oxides (Mn, Co and Ni) underscores the importance of accounting for anharmonic effects in spectral analysis to avoid misinterpretation during material characterization in general.

Methods

Materials

$HClO_4$ (99.999%), $Ni(NO_3)_2 \cdot (H_2O)_6$ (99.999%), $Co(NO_3)_2 \cdot (H_2O)_6$ (EMSURE), $MnCl_2 \cdot (H_2O)_2$ (EMSURE), KCl (EMSURE), KOH (99.99%, semiconductor grade), $LiOH \cdot H_2O$ (99.995%), $NaOH \cdot H_2O$ (99.99%, semiconductor grade) and $CsOH \cdot H_2O$ (99.5%) were purchased from Sigma-Aldrich. Ni sheets (99.99%) were purchased from Mateck. Solutions and electrolytes were prepared with Milli-Q water (18.2 MΩ), except for experiments with isotope-labelled water, that is, D_2O (99.9%) and $H_2^{18}O$ (97%), which were purchased from Deutero. Caro's acid was prepared with 3 parts of 95% H_2SO_4 (technical grade) from VWR chemicals and 1 part of 30% H_2O_2 (for synthesis) from Sigma-Aldrich. Possible Fe impurities in KOH were removed according to the procedure described by Trotochaud et al. for measurements with Ni samples[28]. This procedure involved precipitating $Ni(NO_3)_2$ in 1 M KOH. The precipitated $Ni(OH)_2$ was washed with Milli-Q water and centrifuged. Afterwards, KOH was added to the redispersed $Ni(OH)_2$ and shaken. After a resting period of

at least 3 h, the KOH mixture was centrifuged and subsequently used for measurement. All perfluoroalkoxy alkane (filament; filamentworld), polyvinylidene fluoride (filament; 3Dogg) and glass components were cleaned by soaking in Caro's acid for at least 1 day. Before the experiments, the components were rinsed with and subsequently boiled in ultrapure water at least three times for at least 1 h.

Electrochemical Raman spectroscopy setup

In situ SERS measurements were performed in a perfluoroalkoxy alkane cell (VITLAB GmbH) with a three-dimensional-printed lid made of polyvinylidene fluoride, which is illustrated in Supplementary Fig. 15. The lid had a hole covered by a transparent borosilicate glass disk (Marienfeld), allowing the laser of the Raman spectrometer to interact with the sample. The glass disk was mounted shortly before the start of the experiment to minimize its dissolution in alkaline electrolytes, to prevent silicate contamination. A magnetic stirring bar was included to disperse the bubbles formed during the OER, which limit the Raman measurements at high overpotentials. For measurements in isotope-labelled water (KOD and $K^{18}OH$), a similar cell was used but with a smaller electrolyte volume and without a stirring bar. The stirring bar was used only during measurements in the larger cell under OER conditions, as no effect was observed under other conditions and omitting it ensured consistency between measurements performed in the larger and smaller cells.

The potential was controlled with a PG-285 potentiostat (HEKA-Elektronik), using a leakless Ag/AgCl miniature reference electrode (eDAQ) and a Pt wire (MaTeck, 99.99%) as a counter electrode. The Pt wire was prepared by soaking it in hot acetone (50°C) for at least 0.5 h and subsequently sonicating it in Milli-Q water at room temperature for another 1 h. The Raman spectra were recorded with an inVia confocal Raman microscope (Renishaw) equipped with a charge-coupled device detector, a He–Ne laser with a wavelength of 633 nm (maximum power of 17 mW) and a 50× long working-distance objective.

Sample preparation

The SERS active Ni working electrode (Ni supported on a Au substrate, denoted as Au@Ni) was prepared electrochemically in a glass cell, equipped with a Ag/AgCl (3.4 M) reference electrode and a graphite rod counter electrode. The potential of the working electrode was controlled with a VSP-300 potentiostat from BioLogic. The preparation procedure for the working electrode was adapted from the procedures described by Diaz-Morales et al.[26,82] In short, a Au wire (MaTecK 99.995%) was annealed in a butane flame and then roughened with 30 potential cycles in 0.1 M KCl. Afterwards, deposition was performed in a 5 mM $Ni(NO_3)_2$ and 0.1 M $KClO_4$ solution using a current of 10 µA. For the deposition of Co or Mn, $Co(NO_3)_2 \cdot (H_2O)_6$ or $MnCl_2 \cdot (H_2O)_2$ was used instead. A more detailed procedure can be found in the Supplementary Methods.

Raman spectra processing

The raw Raman spectra were post-processed by adjusting the baseline and removing noise. The baseline was determined with asymmetric least-squares smoothing[83] and subtracted from the signal. Additionally, a Savitzky–Golay filter was applied to all spectra to remove noise[84], which improves the visual separation of peaks from the noise. In all figures, the filtered signal is plotted as a solid line on top of the raw noisy signal (shown with a more transparent colouring).

Measurements performed during different measuring series and during OER conditions can have varying total intensity. To improve comparability, the intensity of each NiO_2 spectrum in the manuscript was scaled so that the maximum of the first peak at 450–480 cm^{-1} has a unified intensity. Peak deconvolution of various SER spectra was performed using the Voigt model from the Python-based lmfit library[85]. To deconvolute the overtone and fundamental modes, their positions were estimated by summing the corresponding fundamental frequencies of the experimentally measured spectrum. A tolerance of ±10 cm^{-1} was allowed to account for possible deviations during the deconvolution process.

Computational methods

All calculations were performed with the Vienna Ab initio Simulation Package 6.2.0[86,87]. The projector augmented wave method was utilized to describe electron–core interactions[88]. In all calculations, plane waves with a cutoff of 600 eV were employed and Gaussian smearing with a width of 0.05 eV was used. The 600-eV cutoff was determined on the basis of a cutoff study for NiOOH (see below), considering both accuracy computational cost. The corresponding values are summarized in Supplementary Table 9.

Bulk structures of $Ni(OH)_2$, NiOOH and NiO_2 were investigated with DFT using the generalized gradient approximation developed by Perdew, Burke and Ernzerhof (PBE) to describe electronic exchange and correlation[89]. Each DFT calculation was performed once with D3 correction[90], and once with Hubbard correction[90] using the approach of Dudarev et al.[91] with a U–J value of 5.5 eV. Similar values have been used in previous reports[15,16,47,60,76]. Furthermore, for all bulk structures, hybrid functional calculations were carried out using PBE0 (with a Hartree–Fock exchange of 25%), HSE06 and B3LYP[92–96]. For $Ni(OH)_2$, a layered brucite-type structure was assumed, consistent with experimental observations[14,20]. The employed unit cells contain two formula units of $Ni(OH)_2$, resulting in a total of ten atoms per cell. To model the β-NiOOH bulk structure, we used a similar framework as for $Ni(OH)_2$, but with half of the hydrogen atoms removed, in line with previous studies[15,20], yielding eight atoms per unit cell. The bulk NiO_2 structure was then obtained by removing the remaining hydrogen atoms from the NiOOH structure, resulting in six atoms per cell. Spin-polarized calculations were performed using a low-spin electronic configuration for the Ni ions, allowing for both ferromagnetic and antiferromagnetic coupling in $Ni(OH)_2$ and NiOOH. Previous reports generally assume that $Ni(OH)_2$ adopts an antiferromagnetic arrangement[31]. For NiOOH, an antiferromagnetic arrangement has also been suggested[59], although ferromagnetic configurations have also been reported[15]. In this work, both ferromagnetic and antiferromagnetic configurations were considered for both materials. The geometry and cell parameters of the three structures were optimized with each of the four above introduced methods, employing a 5 × 3 × 4 **k**-point mesh according to the Monkhorst–Pack scheme[97]. Convergence was achieved when the maximum force applied on any atom is smaller than 0.05 meV $Å^{-1}$, and the energy difference of the electronic self-consistent field was smaller than 10^{-6} eV. The optimized cells yielded stacking orders of ABAB, ABBCCA and ABAB for $Ni(OH)_2$, NiOOH and NiO_2, respectively. Structural parameters can be found in Supplementary Table 2. Density of states were calculated for all bulk structures using a 10 × 6 × 8 **k**-point mesh. To compute formation energies, O_2 and H_2 molecules were calculated for all functionals and formulism described above inside a 30 × 30 × 30 Å cell using a **k**-point mesh of 1 × 1 × 1. Furthermore, calculations were performed for an optimized Ni lattice containing six atoms arranged in a 1 × 3 × 2 rhombohedral lattice ($\alpha = 60°$), corresponding to the face-centred cubic unit cell. Here, a 5 × 3 × 4 **k**-point mesh was employed. The optimized structures are available in the Supplementary Information and ref. 98.

Surface structures of NiOOH and NiO_2 were created using four layers of the optimized bulk structure. Only surfaces calculated with D3 or with Hubbard correction were created owing to the computational cost of hybrid functionals. Each layer consisted of four formula units of either NiOOH or NiO_2, and the positions of the bottom two layers were fixed during geometry optimization. To capture the influence of the surface on the Raman spectra, vacuum was added above each surface slab. The layer-to-layer distances across the vacuum region were 17.6 Å and 18.4 Å for NiOOH and 17.8 Å and 19.4 Å for NiO_2 when calculated with D3 and Hubbard corrections, respectively. Furthermore,

the NiOOH structures were calculated using both ferromagnetic and antiferromagnetic spin configurations. In the antiferromagnetic configuration, each layer itself is antiferromagnetic, where in each layer the two Ni atoms at the smaller x coordinates share the same spin orientation but have opposite spins relative to the two Ni atoms with larger x coordinates. The magnetic moments for the surface structures are of the same order of magnitude as those of the corresponding bulk structures. Phonons were calculated for all structures optimized with D3 or Hubbard corrections using a finite difference approach with a step size of 0.01 Å and a cutoff of 600 eV for the plane wave energy. **k**-points were employed using a $8 \times 4 \times 1$ **k**-point mesh according to the Monkhorst–Pack scheme. To calculate the phonons for the NiOOH and NiO_2 surfaces, the positions of the bottom three layers were fixed and only modes for the top layer were calculated.

Finally, to calculate Raman intensities, an adapted Python script by Fornari and Stauffer was employed, which allows for calculating the macroscopic dielectric tensor with respect to each normal mode by displacing each atom by 0.01 Å along each normal mode vector[99]. Again, for the NiOOH and NiO_2 slabs, only the atoms of the top layer were displaced. Raman intensities were then calculated according to the procedure proposed by Porezag et al.[100] The complete calculated Raman spectra for the bulk and surface structures of NiOOH are shown in Supplementary Fig. 10. Calculations of bulk $Ni(OH)_2$ are presented in Supplementary Fig. 11. Furthermore, the intensity of all calculated phonons and their positions are summarized for each structure in the Supplementary Information.

Data availability

The data supporting the findings of this study are available via Zenodo at https://doi.org/10.5281/zenodo.21899094 (ref. 98).

References

1. Campion, A. & Kambhampati, P. Surface-enhanced Raman scattering. *Chem. Soc. Rev.* **27**, 241–250 (1998).
2. Han, X. X., Rodriguez, R. S., Haynes, C. L., Ozaki, Y. & Zhao, B. Surface-enhanced Raman spectroscopy. *Nat. Rev. Methods Primers* **1**, 87 (2022).
3. Brosseau, C. L. et al. Electrochemical surface-enhanced Raman spectroscopy. *Nat. Rev. Methods Primers* **3**, 79 (2023).
4. Stefancu, A. et al. Impact of surface enhanced Raman spectroscopy in catalysis. *ACS Nano* **18**, 29337–29379 (2024).
5. Itoh, T. et al. Toward a new era of SERS and TERS at the nanometer scale: from fundamentals to innovative applications. *Chem. Rev.* **123**, 1552–1634 (2023).
6. Wang, X., Huang, S.-C., Hu, S., Yan, S. & Ren, B. Fundamental understanding and applications of plasmon-enhanced Raman spectroscopy. *Nat. Rev. Phys.* **2**, 253–271 (2020).
7. Yi, J. et al. Surface-enhanced Raman spectroscopy: a half-century historical perspective. *Chem. Soc. Rev.* **54**, 1453–1551 (2025).
8. Long, D. A. *The Raman Effect: a Unified Treatment of the Theory of Raman Scattering by Molecules* 1st edn (Wiley, 2002)
9. Malard, L. M., Pimenta, M. A., Dresselhaus, G. & Dresselhaus, M. S. Raman spectroscopy in graphene. *Phys. Rep.* **473**, 51–87 (2009).
10. Placidi, M. et al. Multiwavelength excitation Raman scattering analysis of bulk and two-dimensional MoS_2: vibrational properties of atomically thin MoS_2 layers. *2D Mater.* **2**, 035006 (2015).
11. McCrory, C. C. L., Jung, S., Peters, J. C. & Jaramillo, T. F. Benchmarking heterogeneous electrocatalysts for the oxygen evolution reaction. *J. Am. Chem. Soc.* **135**, 16977–16987 (2013).
12. Dionigi, F. & Strasser, P. NiFe-based (oxy)hydroxide catalysts for oxygen evolution reaction in non-acidic electrolytes. *Adv. Energy Mater.* **6**, 1600621 (2016).
13. Bode, H., Dehmelt, K. & Witte, J. Zur kenntnis der nickelhydroxidelektrode—I.Über das nickel (II)-hydroxidhydrat. *Electrochim. Acta* **11**, 1079–1087 (1966).
14. Oliva, P. et al. Review of the structure and the electrochemistry of nickel hydroxides and oxy-hydroxides. *J. Power Sources* **8**, 229–255 (1982).
15. Martirez, J. M. P. & Carter, E. A. Effects of the aqueous environment on the stability and chemistry of β-NiOOH surfaces. *Chem. Mater.* **30**, 5205–5219 (2018).
16. Hu, Q. et al. Structure and oxygen evolution activity of β-NiOOH: where are the protons? *ACS Catal.* **12**, 295–304 (2022).
17. Fidelsky, V., Butera, V., Zaffran, J. & Toroker, M. C. Three fundamental questions on one of our best water oxidation catalysts: a critical perspective. *Theor. Chem. Acc.* **135**, 162 (2016).
18. Kamath, P. V. & Ganguly, S. Infrared spectroscopic studies of the oxide-hydroxides of Ni, Co and Mn. *Mater. Lett.* **10**, 537–539 (1991).
19. Bantignies, J. L. et al. New insight into the vibrational behavior of nickel hydroxide and oxyhydroxide using inelastic neutron scattering, far/mid-infrared and raman spectroscopies. *J. Phys. Chem. C* **112**, 2193–2201 (2008).
20. Glemser, O. & Einerhand, J. Die Struktur höherer Nickelhydroxyde. *Z. Anorg. Chem.* **261**, 43–51 (1950).
21. Kim, M.-S. & Kim, K.-B. A study on the phase transformation of electrochemically precipitated nickel hydroxides using an electrochemical quartz crystal microbalance. *J: Electrochem. Soc.* **145**, 507 (1998).
22. Bediako, D. K. et al. Structure–activity correlations in a nickel–borate oxygen evolution catalyst. *J. Am. Chem. Soc.* **134**, 6801–6809 (2012).
23. Beverskog, B. & Puigdomenech, I. Revised Pourbaix diagrams for nickel at 25–300 °C. *Corros. Sci.* **39**, 969–980 (1997).
24. Huang, L.-F., Hutchison, M. J., Santucci, R. J. Jr, Scully, J. R. & Rondinelli, J. M. Improved electrochemical phase diagrams from theory and experiment: the Ni–water system and its complex compounds. *J. Phys. Chem. C* **121**, 9782–9789 (2017).
25. Sun, W. et al. Insights into the electrochemical oxidation and reduction of nickel oxide surfaces. *ACS Appl. Mater. Interfaces* **17**, 2365–2375 (2025).
26. Diaz-Morales, O., Ferrus-Suspedra, D. & M. Koper, M. T. The importance of nickel oxyhydroxide deprotonation on its activity towards electrochemical water oxidation. *Chem. Sci.* **7**, 2639–2645 (2016).
27. Lee, S., Chu, Y.-C., Bai, L., Chen, H. M. & Hu, X. Operando identification of a side-on nickel superoxide intermediate and the mechanism of oxygen evolution on nickel oxyhydroxide. *Chem Catal.* **3**, 100475 (2023).
28. Trotochaud, L., Young, S. L., Ranney, J. K. & Boettcher, S. W. Nickel–iron oxyhydroxide oxygen-evolution electrocatalysts: the role of intentional and incidental iron incorporation. *J. Am. Chem. Soc.* **136**, 6744–6753 (2014).
29. Louie, M. W. & Bell, A. T. An investigation of thin-film Ni–Fe oxide catalysts for the electrochemical evolution of oxygen. *J. Am. Chem. Soc.* **135**, 12329–12337 (2013).
30. Bernard, M. C. et al. Structural defects and electrochemical reactivity of beta-$Ni(OH)_2$. *J. Power Sources* **63**, 247–254 (1996).
31. Hermet, P. et al. Dielectric, magnetic, and phonon properties of nickel hydroxide. *Phys. Rev. B* **84**, 235211 (2011).
32. Murli, C., Sharma, S. M., Kulshreshtha, S. K. & Sikka, S. K. High-pressure behavior of beta-$Ni(OH)_2$—a Raman scattering study. *Physica B Condensed Matter* **307**, 111–116 (2001).
33. Brooker, M. H., Hancock, G., Rice, B. C. & Shapter, J. Raman frequency and intensity studies of liquid H_2O, $H_2{}^{18}O$ and D_2O. *J. Raman Spectrosc.* **20**, 683–694 (1989).
34. Desilvestro, J., Corrigan, D. A. & Weaver, M. J. Characterization of redox states of nickel hydroxide film electrodes by in situ surface Raman spectroscopy. *J. Electrochem. Soc.* **135**, 885–892 (1988).

35. Yeo, B. S. & Bell, A. T. In situ Raman study of nickel oxide and gold-supported nickel oxide catalysts for the electrochemical evolution of oxygen. *J. Phys. Chem. C* **116**, 8394–8400 (2012).
36. Garcia, A. C., Touzalin, T., Nieuwland, C., Perini, N. & Koper, M. T. M. Enhancement of oxygen evolution activity of nickel oxyhydroxide by electrolyte alkali cations. *Angew. Chem. Int. Ed.* **58**, 12999–13003 (2019).
37. Lee, S., Bai, L. & Hu, X. Deciphering iron-dependent activity in oxygen evolution catalyzed by nickel–iron layered double hydroxide. *Angew. Chem. Int. Ed.* **59**, 8072–8077 (2020).
38. Melendres, C. A., Paden, W., Tani, B. & Walczak, W. On the structure of the higher oxide forms of nickel. *J. Electrochem. Soc.* **134**, 762 (1987).
39. Trześniewski, B. J. et al. In situ observation of active oxygen species in Fe-containing Ni-based oxygen evolution catalysts: the effect of pH on electrochemical activity. *J. Am. Chem. Soc.* **137**, 15112–15121 (2015).
40. Lee, S., Banjac, K., Lingenfelder, M. & Hu, X. Oxygen isotope labeling experiments reveal different reaction sites for the oxygen evolution reaction on nickel and nickel iron oxides. *Angew. Chem.* **131**, 10401–10405 (2019).
41. Michael, J. D. et al. Alkaline electrolyte and Fe impurity effects on the performance and active-phase structure of NiOOH thin films for OER catalysis applications. *J. Phys. Chem. C* **119**, 11475–11481 (2015).
42. Long, D. A. Infrared and Raman characteristic group frequencies. Tables and charts. George Socrates John Wiley and Sons, Ltd, Chichester, third edition, 2001. Price £135. *J. Raman Spectrosc.* **35**, 905 (2004).
43. Hahn, F., Beden, B., Croissant, M. J. & Lamy, C. In situ UV visible reflectance spectroscopic investigation of the nickel electrode–alkaline solution interface. *Electrochim. Acta* **31**, 335–342 (1986).
44. Casas-Cabanas, M. et al. The nickel battery positive electrode revisited: Stability and structure of the β-NiOOH phase. *J. Mater. Chem. A* **6**, 19256–19265 (2018).
45. Kober, F. P. Infrared spectroscopic investigation of charged nickel hydroxide electrodes. *J. Electrochem. Soc.* **114**, 215 (1967).
46. Pushkarev, V. V., Kovalchuk, V. I. & d'Itri, J. L. Probing defect sites on the CeO_2 Surface with dioxygen. *J. Phys. Chem. B* **108**, 5341–5348 (2004).
47. Javad Eslamibidgoli, M., Groß, A. & Eikerling, M. Surface configuration and wettability of nickel(oxy)hydroxides: a first-principles investigation. *Phys. Chem. Chem. Phys.* **19**, 22659–22669 (2017).
48. Li, L.-F., Li, Y.-F. & Liu, Z.-P. Oxygen evolution activity on NiOOH catalysts: four-coordinated Ni cation as the active site and the hydroperoxide mechanism. *ACS Catal.* **10**, 2581–2590 (2020).
49. Wiesner, M. et al. The effect of substrate and surface plasmons on symmetry breaking at the substrate interface of the topological insulator Bi_2Te_3. *Sci. Rep.* **9**, 6147 (2019).
50. Rodriguez, A. et al. Activation of Raman modes in monolayer transition metal dichalcogenides through strong interaction with gold. *Phys. Rev. B* **105**, 195413 (2022).
51. Carpenter, M. K. & Corrigan, D. A. Photoelectrochemistry of nickel hydroxide thin films. *J. Electrochem. Soc.* **136**, 1022 (1989).
52. Varkey, A. J. & Fort, A. F. Solution growth technique for deposition of nickel oxide thin films. *Thin Solid Films* **235**, 47–50 (1993).
53. Croguennec, L., Pouillerie, C., Mansour, A. N. & Delmas, C. Structural characterisation of the highly deintercalated $Li_xNi_{1.02}O_2$ phases (with $x \leq 0.30$). *J. Mater. Chem.* **11**, 131–141 (2001).
54. Togonon, J. J. H. et al. Insights into the role of the covalent Ni–O bonds in $Lino_2$ positive electrodes: a correlative hard X-ray spectroscopy study. *J. Mater. Chem. A* **13**, 28305–28317 (2025).
55. Fantin, R. et al. Depth-resolving the charge compensation mechanism from $LiNiO_2$ to NiO_2. *ACS Energy Lett.* **9**, 1507–1515 (2024).
56. Wani, A. F., Rani, B., Sharopov, U. B., Dhiman, S. & Kaur, K. Thermoelectric investigation of transition metal oxide NiO_2: a first principles study. *Int. J. Energy Res.* **46**, 8527–8535 (2022).
57. Pandya, K. I., Hoffman, R. W., McBreen, J. & O'Grady, W. E. In situ X-ray absorption spectroscopic studies of nickel oxide electrodes. *J. Electrochem. Soc.* **137**, 383 (1990).
58. Farley, N. R. S., Gurman, S. J. & Hillman, A. R. Dynamic EXAFS study of discharging nickel hydroxide electrode with non-integer Ni valency. *Electrochim. Acta* **46**, 3119–3127 (2001).
59. Tkalych, A. J., Yu, K. & Carter, E. A. Structural and electronic features of β-$Ni(OH)_2$ and β-NiOOH from first principles. *J. Phys. Chem. C* **119**, 24315–24322 (2015).
60. Zaffran, J. & Caspary Toroker, M. Benchmarking density functional theory based methods to model NiOOH material properties: Hubbard and van der Waals corrections vs hybrid functionals. *J. Chem. Theory Comput.* **12**, 3807–3812 (2016).
61. Morishita, M. et al. Phase transformation in the charge–discharge process and the structural analysis by synchrotron XAFS and XRD for nickel hydroxide electrode. *Electrochemistry* **76**, 802–807 (2008).
62. Friebel, D. et al. Identification of highly active Fe sites in (Ni,Fe) OOH for electrocatalytic water splitting. *J. Am. Chem. Soc.* **137**, 1305–1313 (2015).
63. Görlin, M. et al. Oxygen evolution reaction dynamics, faradaic charge efficiency, and the active metal redox states of Ni–Fe oxide water splitting electrocatalysts. *J. Am. Chem. Soc.* **138**, 5603–5614 (2016).
64. Zhao, T. et al. In situ reconstruction of V-doped Ni_2P pre-catalysts with tunable electronic structures for water oxidation. *Adv. Funct. Mater.* **31**, 2100614 (2021).
65. Balasubramanian, M., Melendres, C. A. & Mini, S. X-ray absorption spectroscopy studies of the local atomic and electronic structure of iron incorporated into electrodeposited hydrous nickel oxide films. *J. Phys. Chem. B* **104**, 4300–4306 (2000).
66. Angermann, M. et al. Highly conductive RuO_2 thin films from novel facile aqueous chemical solution deposition. *J. Sol-Gel Sci. Technol.* **108**, 575–587 (2023).
67. Kalantar-zadeh, K. et al. Two dimensional and layered transition metal oxides. *Appl. Mater. Today* **5**, 73–89 (2016).
68. Bhattacharyya, D. et al. Vibrational Stark shift spectroscopy of catalysts under the influence of electric fields at electrode–solution interfaces. *Chem. Sci.* **12**, 10131–10149 (2021).
69. Zou, S. & Weaver, M. J. Potential-dependent metal-adsorbate stretching frequencies for carbon monoxide on transition-metal electrodes: chemical bonding versus electrostatic field effects. *J. Phys. Chem.* **100**, 4237–4242 (1996).
70. Glemser, O. & Einerhand, J. Über höhere Nickelhydroxyde. *Z. anorg. Chemie* **261**, 26–42 (1950).
71. Corrigan, D. A. & Knight, S. L. Electrochemical and spectroscopic evidence on the participation of quadrivalent nickel in the nickel hydroxide redox reaction. *J. Electrochem. Soc.* **136**, 613–619 (1989).
72. Trzesniowski, H. et al. Reversible and irreversible cation intercalation in $NiFeO_x$ oxygen evolution catalysts in alkaline media. *J. Phys. Chem. Lett.* **14**, 545–551 (2023).
73. O'Grady, W. E., Pandya, K. I., Swider, K. E. & Corrigan, D. A. In situ X-ray absorption near-edge structure evidence for quadrivalent nickel in nickel battery electrodes. *J. Electrochem. Soc.* **143**, 1613 (1996).
74. Gallenberger, J. et al. Stability and decomposition pathways of the NiOOH OER active phase of NiO_x electrocatalysts at open circuit potential traced by ex situ and in situ spectroscopies. *Catal. Sci. Technol.* **13**, 4693–4700 (2023).
75. Chan, H. Y. H., Takoudis, C. G. & Weaver, M. J. Oxide film formation and oxygen adsorption on copper in aqueous media as probed by surface-enhanced Raman spectroscopy. *J. Phys. Chem. B* **103**, 357–365 (1999).

76. Tkalych, A. J., Zhuang, H. L. & Carter, E. A. A density functional + *U* assessment of oxygen evolution reaction mechanisms on β-NiOOH. *ACS Catal.* **7**, 5329–5339 (2017).
77. Govind Rajan, A., Martirez, J. M. P. & Carter, E. A. Facet-independent oxygen evolution activity of pure β-NiOOH: different chemistries leading to similar overpotentials. *J. Am. Chem. Soc.* **142**, 3600–3612 (2020).
78. Son, Y. J. et al. Key concepts for understanding alkaline oxygen evolution reaction at the atomic/molecular scalea. *Curr. Opin. Electrochem.* **39**, 101298 (2023).
79. Binninger, T. & Doublet, M.-L. The Ir–OOOO–Ir transition state and the mechanism of the oxygen evolution reaction on IrO_2(110). *Energy Environ. Sci.* **15**, 2519–2528 (2022).
80. Wei, J. et al. Sequential oxygen evolution and decoupled water splitting via electrochemical redox reaction of nickel hydroxides. *Nat. Commun.* **15**, 9012 (2024).
81. Zaffran, J. & Toroker, M. C. Understanding the oxygen evolution reaction on a two-dimensional NiO_2 catalyst. *ChemElectroChem* **4**, 2764–2770 (2017).
82. Gao, P., Gosztola, D., Leung, L.-W. H. & Weaver, M. J. Surface-enhanced Raman scattering at gold electrodes: dependence on electrochemical pretreatment conditions and comparisons with silver. *J. Electroanal. Chem. Interfacial Electrochem.* **233**, 211–222 (1987).
83. Eilers, P. H. & Boelens, H. F. Baseline correction with asymmetric least squares smoothing. Leiden University Medical Centre Report (2005).
84. Savitzky, A. & Golay, M. J. E. Smoothing and differentiation of data by simplified least squares procedures. *Anal. Chem.* **36**, 1627–1639 (1964).
85. Newville, M. et al. LMFIT: non-linear least-squares minimization and curve-fitting for Python. *Zenodo* https://doi.org/10.5281/zenodo.16175987 (2025).
86. Kresse, G. & Furthmüller, J. Efficiency of ab-initio total energy calculations for metals and semiconductors using a plane-wave basis set. *Comput. Mater. Sci.* **6**, 15–50 (1996).
87. Kresse, G. & Furthmüller, J. Efficient iterative schemes for ab initio total-energy calculations using a plane-wave basis set. *Phys. Rev. B* **54**, 11169–11186 (1996).
88. Blöchl, P. E. Projector augmented-wave method. *Phys. Rev. B* **50**, 17953–17979 (1994).
89. Perdew, J. P., Burke, K. & Ernzerhof, M. Generalized gradient approximation made simple. *Phys. Rev. Lett.* **77**, 3865–3868 (1996).
90. Grimme, S., Antony, J., Ehrlich, S. & Krieg, H. A consistent and accurate ab initio parametrization of density functional dispersion correction (DFT-D) for the 94 elements H–Pu. *J. Chem. Phys.* **132**, 154104 (2010).
91. Dudarev, S. L., Botton, G. A., Savrasov, S. Y., Humphreys, C. J. & Sutton, A. P. Electron-energy-loss spectra and the structural stability of nickel oxide: an LSDA+*U* study. *Phys. Rev. B* **57**, 1505–1509 (1998).
92. Perdew, J. P., Ernzerhof, M. & Burke, K. Rationale for mixing exact exchange with density functional approximations. *J. Chem. Phys.* **105**, 9982–9985 (1996).
93. Ernzerhof, M. & Scuseria, G. E. Assessment of the Perdew–Burke–Ernzerhof exchange–correlation functional. *J. Chem. Phys.* **110**, 5029–5036 (1999).
94. Adamo, C. & Barone, V. Toward reliable density functional methods without adjustable parameters: the PBE0 model. *J. Chem. Phys.* **110**, 6158–6170 (1999).
95. Krukau, A. V., Vydrov, O. A., Izmaylov, A. F. & Scuseria, G. E. Influence of the exchange screening parameter on the performance of screened hybrid functionals. *J. Chem. Phys.* **125**, 224106 (2006).
96. Stephens, P. J., Devlin, F. J., Chabalowski, C. F. & Frisch, M. J. Ab initio calculation of vibrational absorption and circular dichroism spectra using density functional force fields. *J. Phys. Chem.* **98**, 11623–11627 (1994).
97. Monkhorst, H. J. & Pack, J. D. Special points for Brillouin-zone integrations. *Phys. Rev. B* **13**, 5188–5192 (1976).
98. Leist, J. et al. Data of Consequences of overtones in Raman spectra for assigning nickel anode surface structures as NiO2 during alkaline electrolysis. *Zenodo* https://doi.org/10.5281/zenodo.21899094 (2026).
99. Fonari, A. & Stauffer, S. Raman-sc/VASP (raman-sc, 2013).
100. Porezag, D. & Pederson, M. R. Infrared intensities and Raman-scattering activities within density-functional theory. *Phys. Rev. B* **54**, 7830–7836 (1996).

Acknowledgements

The authors gratefully acknowledge computational resources provided by the state of Baden-Württemberg through bwHPC.

Author contributions

J.L.: conceptualization, formal analysis, investigation (experiments and theory), data curation, validation, visualization, writing—original draft preparation. A.N.: investigation (theory), validation, writing—review and editing. T.J.: funding acquisition, resources supervision, writing—review and editing. A.K.E.: funding acquisition, conceptualization, supervision, writing—review and editing.

Funding

This work was funded by the German Research Foundation (DFG) through Collaborative Research Centre CRC 1316 (project 327886311) and through grant no. INST 40/575-1 FUGG (JUSTUS 2 cluster).Open access funding provided by Universität Ulm.

Competing interests

The authors declare no competing interests.

Additional information

Supplementary information The online version contains supplementary material available at https://doi.org/10.1038/s41929-026-01613-9.

Correspondence and requests for materials should be addressed to Timo Jacob or Albert K. Engstfeld.

Peer review information *Nature Catalysis* thanks the anonymous reviewers for their contribution to the peer review of this work. Peer reviewer reports are available.